© 2018 IEEE. Personal use of this material is permitted. Permission from IEEE must be obtained for all other uses, in any current or future media, including reprinting/republishing this material for advertising or promotional purposes, creating new collective works, for resale or redistribution to servers or lists, or reuse of any copyrighted component of this work in other works.

A Tuned Lightweight Estimation Algorithm for Low-cost Phasor Measurement Units

Pietro Tosato*, *Student Member, IEEE,* David Macii*, *Senior Member, IEEE,* Mario Luiso†, *Member, IEEE,* Davide Brunelli*, *Senior Member, IEEE,* Daniele Gallo†, *Member, IEEE,* Carmine Landi† *Member, IEEE,*

*Department of Industrial Engineering
University of Trento, Trento, Italy
Email: {david.macii}@unitn.it
†Department of Industrial and Information Engineering
University of Campania "L. Vanvitelli"
Aversa (CE), Italy
Email: mario.luiso@unicampania.it

***Abstract*—Nowadays, the interest in low-cost and increasingly accurate Phasor Measurement Units (PMUs) for active distribution systems is steadily growing. In this paper, an algorithm for synchrophasor, fundamental frequency and ROCOF estimation tailored for processing platforms with limited computational resources is described and characterized extensively in terms of both accuracy and processing time. The proposed solution harnesses the main advantages of two state-of-the-art algorithms, i.e. the Interpolated Discrete Fourier Transform (IpDFT) and the Taylor-Fourier Transform (TFT). Such algorithms are combined and implemented in a computationally-efficient manner to reduce processing time as much as possible, while ensuring good accuracy in the main testing conditions specified in the IEEE Standard C37.118.1-2011 and its Amendment C37.118.1a-2014. Estimation accuracy has been evaluated not only through simulations, but also experimentally. The good consistency between simulation-based and experimental results provides clear evidence that the uncertainty contributions due to transducers, acquisition and synchronization systems can be reasonably kept under control. The processing times of the algorithm, implemented on an embedded platform suitable for PMU prototyping, are compliant with the mandatory reporting rates of Class M PMUs.**

Keywords*—Phasor Measurement Unit (PMU), power system monitoring, signal processing algorithms, embedded systems, power systems measurements, estimation error.

I. Introduction

Phasor Measurement Units (PMUs) are instruments able to measure amplitude, phase, frequency and rate of change of frequency (ROCOF) of voltage or current waveforms at times synchronized to the Coordinated Universal Time (UTC) [1]. Generally speaking, PMUs are used to improve grid observability. At the transmission level, the measurement data acquired by multiple PMUs and collected through Wide Area Monitoring (WAM) systems are finally aligned in time by the so-called Phasor Data Concentrators (PDCs) to estimate the state of the grid at a given time [2]. In this way, Transmission Systems Operators (TSOs) can constantly monitor grid stability, detect and analyze faults, monitor dynamic load or line conditions and support power system restoration [3].

With the advent of active distribution grids and the progressive shift from unidirectional to bidirectional power flow schemes, measurement instruments such as the PMUs have become increasingly interesting also for Distribution Systems Operators (DSOs) [4], [5]. In particular, the penetration of generators based on distributed energy resources (DERs) (e.g. photovoltaic systems, wind farms or storage systems) as well as the diffusion of strongly non-linear and time-varying loads (e.g. plug-in electric vehicles) requires a widespread deployment of measurement and monitoring systems able to guarantee reliable and safe grid operation, even when the amount of power exchanged between "prosumers" becomes substantial. In addition, critical power quality (PQ) events in distribution systems have to be promptly detected [6]–[8].

Unfortunately, cost and infrastructural constraints limit the deployment of PMUs in distribution grids. This problem can be partially tackled with optimal placement strategies [9]–[11]. However, crucial performance issues still exist due to the intrinsic differences between transmission and distribution systems. The latter are indeed affected by significant imbalances, larger harmonic distortion, and uncertain line parameters [12]–[14]. Moreover, shorter line length and lower power flows make the angle differences between voltage bus or line current phasors very small (i.e. in the order of a few mrad or less), which requires higher phase measurement accuracy than in transmission systems [15], [16]. One of the most known examples of PMU for distribution grids is probably the micro-PMU by PSL [17]. However, the implementation details of this instrument are not disclosed. The PMU prototype described in [15] is based on a Field Programmable Gate Array (FPGA) to maximize the execution speed when the sampling rate is very high (up to 50 kSa/s). Despite this, the chosen hardware platform (i.e. a NI CRIO) is still quite expensive. Therefore, cheaper and, despite this, more accurate PMUs are needed in the future. Unfortunately, low cost and high accuracy are usually contrasting goals. The accuracy problem can be mitigated by using increasingly sophisticated estimation algorithms, although voltage and current measurement transducers

doi: 10.1109/TIM.2017.2775458

still have a crucial impact on metrological performance [18]–[20]. On the other hand, a higher computational complexity requires more powerful and expensive processing platforms able to sustain real-time reporting rates in the order of tens of frames per second [21], [22]. Of course, this issue impacts on hardware costs and it is further exacerbated by a complementary aspect, i.e. the need to keep the sampling frequency reasonably low (i.e. between a few kHz and a few tens of kHz), while maximizing the effective resolution of the data acquisition stage. In fact, the sensitivity to wideband noise increases as the number of parameters to be estimated grows, as confirmed by the fact that the Cramer-Rao Lower Bounds (CRLB) of such quantities tend to increase accordingly [23].

In this involved scenario, this paper presents a solution able to achieve a good trade-off between estimation accuracy and computational burden. The proposed technique relies on the combination of two state-of-the-art algorithms, i.e. the Interpolated Discrete Fourier Transform (IpDFT) and the real-valued Taylor-Fourier Transform (TFT), which are combined and implemented in a computationally-efficient way to ensure real-time operation in low-cost processing platforms.

The rest of the paper is structured as follows. First, in Section II the state-of-the-art about synchrophasor estimation algorithms is briefly recalled. Then, in Section III the proposed estimation technique is explained in detail. Section IV reports both simulation and experimental results in the main steady-state and dynamic testing conditions reported in the IEEE Standards C37.118.1-2011 and C37.118.1a-2014 [21], [24]. Finally, Section V describes the implementation of the proposed estimation algorithm using a BeagleBone Black board and shows the reduction in processing time with respect to the solution presented in [25].

II. Related Work

Many techniques for synchrophasor estimation have been developed over the last few years. The estimators based on a *static* synchrophasor model rely on the assumption that a phasor referred to a given UTC time is constant over the whole data record used to estimate the quantities of interest. Three classic approaches that stem from this general assumption are: the classic windowed DFT [26], the IpDFT algorithm [27], and the technique described in Annex C of the IEEE Standard C37.118.1-2011 [21], which is also adopted by most of instrument manufacturers. In particular, this technique is based on the direct down-conversion of a 50-Hz or 60-Hz digitized waveform followed by the low-pass filtering of the resulting in-phase and quadrature waveform components. The accuracy of this measurement technique strongly depends on the features of the chosen filters [28]. In this respect, excellent performance can be achieved by using adaptive filters for harmonics cancellation based on fundamental frequency tracking [29], [30]. While the *static* synchrophasor model is definitely suitable for PMUs designed for transmission systems, the case of distribution systems is still unclear, as the performance requirements at the distribution level are still undefined. At the moment, it is just widely accepted in the scientific community that the PMUs for distribution systems should be able to better track variations of amplitude, phase and frequency. Also, phase measurement accuracy should be particularly high. For this reason, the so-called *dynamic* synchrophasor model has been recently adopted. According to this model, a synchrophasor is no longer assumed, nor required to be in a steady-state over a given observation interval. On the contrary, amplitude, phase and frequency of the fundamental are regarded as generic functions of time. Since no univocal models exist to describe the evolution of a synchrophasor over time, an effective approach is to approximate the synchrophasor function with its Taylor's series centered at the chosen reference time and truncated to order K. In this way, the synchrophasor behavior can be reconstructed by estimating the coefficients of the Taylor's series, i.e. the derivatives of the synchrophasor function from order 0 to K. Such coefficients can be estimated through weighted least squares (WLS) fitting [31], [32], finite difference equations [33] or in the frequency domain using different samples of the DFT around the fundamental [34].

The same approach can be also extended to estimate the most significant harmonics through the so-called Taylor-Fourier Transform (TFT) [35]. The TFT has been implemented in a variety of ways, e.g. through least squares fitting in the time domain or using a bank of multiple resonators in the frequency domain [36]. More recently, the Taylor-Fourier analysis has been used to define various discrete-time dynamic models. As a result, different Taylor-Kalman filters (TKF) have been implemented [37]–[39]. Unfortunately, both the TFT and the TKF can be strongly affected by inter-harmonics. In addition, the TKF is more sensitive than the TFT to possible disturbances which are not included in the waveform model [40].

To address the out-of-band inter-harmonic problem, an algorithm based on the combination of TFT and Compressed Sensing (CS) is described in [41]. This algorithms detects the most harmful inter-harmonic contributions and estimates their frequencies prior to applying the TFT. The main drawback of this solution is its computational complexity, which grows with the number of harmonics and inter-harmonics terms included in the model.

The estimation technique described in this paper still relies on a TFT, but it blends the results of other research works to propose a solution characterized by an optimal trade-off between accuracy, robustness to unmodelled disturbances and processing time. First of all, unlike the classic TFT, the coefficients of the system matrix are tuned at run-time through a preliminary estimation of the the static off-nominal frequency deviation of the fundamental, which results from a preliminary IpDFT. The idea of tuning the coefficients of the TFT system matrix is not totally new, as it was used also in [32]. However, the IpDFT is computationally light, it is not iterative and it returns a very accurate estimate of the frequency bin corresponding to the spectral peak of a sinewave once other disturbances are filtered. Moreover, since one of the inherent IpDFT uncertainty sources is the spectral leakage from the image component of the fundamental, a Maximum Image Rejection (MIR) window is used [26]. In addition, the number of unknowns to be estimated by the

TFT is minimized as a function of the observation interval length, since just the most critical harmonics are retained in the waveform model. Compared with the algorithm presented in [25], the TFT has been completely reformulated using real-valued instead of complex-valued quantities, thus drastically reducing the computational burden, as it will be shown in Section V. For this reason, in this paper the overall algorithm will be shortly referred to as *Tuned Lightweight Taylor Fourier Transform* (TLTFT).

III. Waveform Model and Estimation Algorithm

Given a voltage or current waveform sampled at a rate $f_s = M \cdot f_0$ (where f_0 is the nominal fundamental frequency and $M \in \mathbb{N}$), the data record collected in an observation interval centered at reference time $t_r = \frac{r}{f_s}$ and consisting of $N = C \cdot M$ samples (with C being an integer number of waveform cycles at frequency f_0) can be modeled as

$$x(n)=X(n)\cos\varphi(n)+\varepsilon_h(n)+\eta(n) \tag{1}$$

for $r - \frac{N-1}{2} \leq n \leq r + \frac{N-1}{2}$ (if N is odd) or $r - \frac{N}{2} \leq n \leq r + \frac{N}{2} - 1$ (if N even), where

$$\begin{aligned} X(n) &= X[1+\varepsilon_a(n)] \\ \varphi(n) &= 2\pi\frac{f}{f_s}n+\varepsilon_p(n)+\phi \end{aligned} \tag{2}$$

are the waveform amplitude and phase, respectively, at the nth sampling time in the observation interval considered, X is the nominal waveform amplitude, $f = f_0 \cdot (1+\delta)$ is the fundamental frequency (which can be affected by a fractional off-nominal deviation δ), ϕ is the initial phase at time t_r, $\varepsilon_a(n)$ and $\varepsilon_p(n)$ represent possible amplitude and phase fluctuations, $\varepsilon_h(n)$ includes harmonic and inter-harmonic disturbances, and finally $\eta(n)$ models the total additive wideband noise (e.g. due to both acquisition and synchronization circuitry) [42]. As known, a PMU is supposed to measure synchrophasor, frequency and ROCOF of the fundamental of (1) at time t_r, i.e.

$$\bar{X}(t_r)=\frac{X(t_r)}{\sqrt{2}}e^{j\varphi(t_r)},\ f(t_r)=\left.\frac{d\varphi(t)}{dt}\right|_{t_r},\ ROCOF(t_r)=\left.\frac{d^2\varphi(t)}{dt^2}\right|_{t_r}. \tag{3}$$

According to the IEEE Standard C37.118.1-2011 and its Amendment C37.118.1a-2014 [21], [24], PMU accuracy is expressed in terms of *Total Vector Error* (TVE), i.e.

$$TVE(t_r) = \frac{|\hat{X}(t_r)e^{j\hat{\varphi}(t_r)} - X(t_r)e^{j\varphi(t_r)}|}{|X(t_r)e^{j\varphi_r(t_r)}|}; \tag{4}$$

Frequency Error (FE), i.e.

$$FE(t_r)=|\hat{f}(t_r) - f(t_r)|; \tag{5}$$

and *Rate of Change of Frequency Error* (RFE), i.e.

$$RFE(t_r) = |\widehat{ROCOF}(t_r) - ROCOF(t_r)|. \tag{6}$$

Observe that, here and in the rest of the paper, symbol $\hat{\cdot}$ denotes the corresponding estimated quantity.

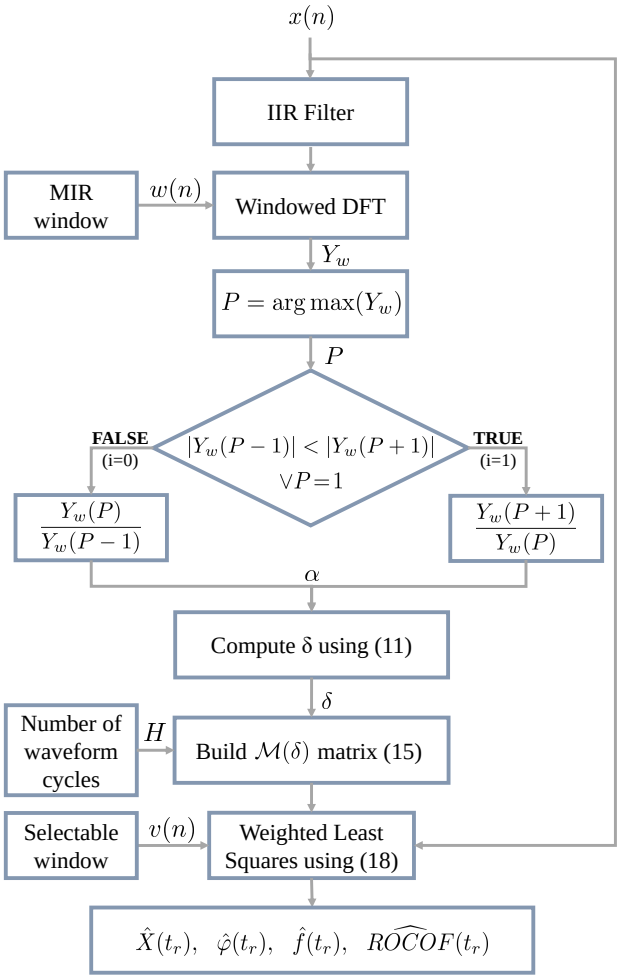

Fig. 1. Flow chart of the TLTFT estimation algorithm.

As shortly explained in Section II, the TLTFT algorithm (whose flow chart is shown in Fig. 1) consists of two main steps, which are described in detail in the following subsections.

A. Estimation of the Static Frequency Deviation

The purpose of the first step of the TLTFT algorithm is to estimate and compensate for the effect of the off-nominal static frequency deviation δ. In this way, the matrix coefficients of the following TFT step can be tuned as a function of the estimated fundamental frequency, as explained in Section III-B. Such a frequency is estimated by a windowed IpDFT algorithm. Before the IpDFT, a filter with the following specifications is used:

- Lower/upper passband frequencies: 45 Hz and 55 Hz;
- Lower/upper stopband frequencies: 10 Hz and 90 Hz;
- Minimum frequency response magnitude in the passband: -0.009 dB;
- Maximum attenuation in the stopband: 34 dB;

in order to mitigate the effect of disturbances $\varepsilon_h(n)$ and $\eta(n)$ on δ estimation. Observe that the filter passband is purposely set equal to the off-nominal frequency range of *M Class* PMUs [21], whereas the stopband edge frequencies are chosen so as to relax the transition bandwidth, while ensuring high harmonics rejection. In this way, the fundamental component of the collected waveform is basically unaltered. To keep the filter order as low as possible, an Infinite Input Response (IIR) elliptic filter is used. The rationale for this choice is that, for given filter specifications, this kind of digital filters exhibits a lower order (6 in the case at hand) than other IIR or Finite Impulse Response (FIR) filters. Moreover, the order of standard IIR filters as well as their computational burden are independent of the sampling frequency. Therefore, their coefficients can be easily adapted to different values of f_s, without redesigning the filter. The proposed elliptic filter can be effectively implemented with a canonical (i.e. direct form II) structure which requires just a few multiply-accumulate (MAC) operations for each new collected sample. Consider that, due to its low order, no numerical stability problems arise.

A major drawback of IIR and, particularly, elliptic filters is their severe in-band phase distortion. However, this problem does not affect the accuracy of the TLTFT algorithm. Indeed, the filter is used just to clean up the signal before applying the IpDFT for δ estimation, but it is not used directly for synchrophasor estimation. On the contrary, the TFT (namely the core of the algorithm described in Section III-B) is applied directly to the unfiltered $x(n)$ signal, as highlighted by the bypass edge connecting $x(n)$ with the WLS block in Fig. 1. Moreover, as explained below, the estimation of δ through the IpDFT depends just on the magnitude spectrum of the filtered signal. Thus, the filter phase response has no effect on results. The group delay and the initial transient of the filter are not a problem as well, because δ is assumed to be static, i.e. almost constant over multiple cycles.

Let us assume that, without loss of generality, N is an odd number. If $y(n)$ for $r-\frac{N-1}{2} \leq n \leq r+\frac{N-1}{2}$ denotes the waveform resulting from the filtering of (1) and if

$$w(n) = \frac{4C^2}{8C^2-1} + \frac{4C^2-1}{8C^2-1}\cos\left(\frac{2\pi}{N}n\right) \tag{7}$$

is the MIR window sequence over C cycles [26], the windowed DFT of $y(n)$ over N samples is given by

$$Y_w(k) = \frac{1}{N}\sum_{n=-\frac{N-1}{2}}^{\frac{N-1}{2}} w(n)y(n)e^{-j2\pi\frac{kn}{N}} \quad k=0,\ldots,N-1. \tag{8}$$

Let P be the frequency bin corresponding to the magnitude spectrum peak associated with the fundamental component of $y(n)$. In principle, waveform sampling should be coherent, but this is not actually possible in the presence of some off-nominal frequency deviation. If $|C\delta| \leq 1$, then $P = C$. Otherwise, if $|C\delta| > 1$, then P is set equal to $C+1$ or $C-1$, respectively, depending on whether the fractional frequency deviation is positive or negative. If the disturbances in (1) are properly filtered and if the spectral leakage due to the image component has a negligible impact on the spectral peak of the fundamental, then it can be shown that [27]

$$\alpha = \frac{|Y_w(P+i)|}{|Y_w(P-1+i)|} \approx \frac{|W(i-P\delta)|}{|W(-1+i-P\delta)|} \tag{9}$$

where $W(\cdot)$ is the Discrete-Time Fourier Transform (DTFT) of (7) and

$$i = \begin{cases} 0 & |Y_w(P-1)| \geq |Y_w(P+1)| \\ 1 & |Y_w(P-1)| < |Y_w(P+1)| \vee P=1. \end{cases} \tag{10}$$

Note that if $P = 1$, then i is always set equal to 1 to avoid using $|Y_w(0)|$, which can be strongly affected by spectral leakage. Observe that the rightmost term of (9) is a non-linear function of δ. Therefore, the value of δ can be estimated by solving equation (9). In the case of MIR windows, the static off-nominal fractional frequency offset can be computed using the following approximate expression, i.e. [43]

$$\hat{\delta} \cong \begin{cases} \frac{1}{C}\left[P-C+2\sqrt{p}\cos(\frac{\pi}{3}+\frac{\psi}{3})-\frac{\alpha+2}{3(\alpha+1)}\right] & i=0 \\ \frac{1}{C}\left[P-C-2\sqrt{p}\cos(\frac{\pi}{3}+\frac{\psi}{3})+\frac{\alpha+2}{3(\alpha+1)}\right] & i=1 \end{cases} \tag{11}$$

where $p = \frac{12C^2+4}{9} - \frac{\alpha}{9(\alpha+1)^2}$, and $\psi = \cos^{-1}\left(\frac{|u|}{p\sqrt{p}}\right)$ with $u = \frac{(\alpha-1)[(\alpha+1)^2(144C^2-16)+\alpha]}{54(\alpha+1)^3}$. The value of $\hat{\delta}$ given by (11) can be eventually used to tune the coefficients of the TFT, as it will be explained in the next subsection.

B. Estimation of Synchrophasor, Frequency and ROCOF

In the classic TFT, the synchophasor Taylor's series of both the fundamental tone and its harmonics till a specified order H are used to model the waveform evolution over time within a given observation intervals centered at the reference instant. In the following, the TFT has been enhanced in two ways. First of all, the TFT estimator is reformulated by splitting the real and imaginary parts of the corresponding synchrophasors, in order to process just real-valued rather than complex-valued quantities. Secondly, the number H of harmonic terms included in the waveform model is chosen adaptively as a function of the observation interval length, in view of reducing processing time as much as possible. Assuming that inter-harmonics and wideband noise contributions in (1) are negligible and that only H harmonics are considered in $\varepsilon_h(n)$, then (1) can be rewritten as follows, i.e.

$$x(n) = \sum_{h=1}^{H} X_R^{(h)}\cos\left(2\pi h\frac{f}{f_s}n\right) - X_I^{(h)}\sin\left(2\pi h\frac{f}{f_s}n\right) \tag{12}$$

where, again, $r-\frac{N-1}{2} \leq r+n \leq \frac{N-1}{2}$ (for N odd), $f = f_0\cdot(1+\delta)$, $X_R^{(h)}$ and $X_I^{(h)}$ are the real and imaginary parts of the phasor of the hth harmonic at reference time t_r, respectively, i.e. $\bar{X}^{(h)} = X_R^{(h)} + jX_I^{(h)}$. Of course, $\bar{X}^{(1)} = \bar{X}$ is the synchrophasor of the fundamental, as defined in (3). Let

$$X_R^{(h)} \approx \sum_{k=1}^{K_h} X_{R_k}^{(h)}(n-r)^k \quad \text{and} \quad X_{I_k}^{(h)} \approx \sum_{k=1}^{K_h} X_{I_k}^{(h)}(n-r)^k \tag{13}$$

with $X_{R_k}^{(h)}=\frac{1}{k!(Mf_0)^k}\left.\frac{d^k X_R^{(h)}}{dt^k}\right|_{t_r}$ and $X_{I_k}^{(h)}=\frac{1}{k!(Mf_0)^k}\left.\frac{d^k X_I^{(h)}}{dt^k}\right|_{t_r}$ be the Taylor's series of $X_R^{(h)}$ and $X_I^{(h)}$, respectively. If the Taylor's series coefficients are orderly rearranged in the vector $\mathbf{X}=[\mathbf{X}^{(1)},\ldots,\mathbf{X}^{(H)}]^T$ where $\mathbf{X}^{(h)}=[X_{R_{K_h}}^{(h)},\ldots,X_{R_0}^{(h)},-X_{I_0}^{(h)},\ldots,-X_{I_{K_h}}^{(h)}]^T$ for $h=1,\ldots,H$, by substituting (13) into (12), after some algebraic steps [35], the sequence of values $x(n)$ can be expressed in a matrix form as follows, i.e.

$$\mathbf{x}=\mathcal{M}(\delta)\mathbf{X}, \tag{14}$$

where $\mathbf{x}$ is a $1\times N$ vector comprising the samples collected in the observation interval considered and

$$\mathcal{M}(\delta)=\begin{bmatrix} A_{K_1}^{(1)}(\delta) & B_{K_1}^{(1)}(\delta) & \cdots & A_{K_H}^{(H)}(\delta) & B_{K_H}^{(H)}(\delta) \\ \Gamma_{K_1}^{(1)}(\delta) & \Delta_{K_1}^{(1)}(\delta) & \cdots & \Gamma_{K_H}^{(H)}(\delta) & \Delta_{K_H}^{(H)}(\delta) \end{bmatrix} \tag{15}$$

is a $N\times 2\cdot(K_1+...+K_H+H)$ real-valued matrix whose elements for $h=1,\ldots,H$ are functions of δ and are defined as follows, i.e.

$$\begin{aligned}\left(A_{K_h}^{(h)}(\delta)\right)_{lq}&=\left(l-\frac{N+1}{2}\right)^{K_h-q}\cos\left[\frac{2\pi h(1+\delta)}{M}\left(\frac{N+1}{2}-l\right)\right],\\ \left(B_{K_h}^{(h)}(\delta)\right)_{lq}&=-\left(l-\frac{N+1}{2}\right)^{q}\sin\left[\frac{2\pi h(1+\delta)}{M}\left(\frac{N+1}{2}-l\right)\right],\end{aligned} \tag{16}$$

for $q=0,...,K_h$ and $l=1,...,\frac{N+1}{2}$, while

$$\begin{aligned}\left(\Gamma_{K_h}^{(h)}(\delta)\right)_{lq}&=l^{K_h-q}\cos\left[\frac{2\pi h(1+\delta)}{M}l\right],\\ \left(\Delta_{K_h}^{(h)}(\delta)\right)_{lq}&=l^{q}\sin\left[\frac{2\pi h(1+\delta)}{M}l\right],\end{aligned} \tag{17}$$

for $q=0,...,K_h$ and $l=1,...,\frac{N-1}{2}$.

Therefore, if the coefficients of $\mathcal{M}(\delta)$ are tuned using the value $\hat{\delta}$ returned by (11), and if (12) is windowed by a suitable function $v(\cdot)$ (which in general can be different from (7)) to smooth the Taylor's series approximation errors at the boundaries of the observation interval considered, the elements of the unknown vector can be estimated by using a Weighted Least Squares (WLS) approach, i.e.

$$\hat{\mathbf{X}}=\left[\mathcal{M}(\hat{\delta})^T V^T V\mathcal{M}(\hat{\delta})\right]^{-1}\mathcal{M}(\hat{\delta})^T V^T V\mathbf{x}, \tag{18}$$

where $V=\mathrm{diag}\{v(0),\ldots,v(N-1)\}$ is the $N\times N$ diagonal matrix built using the coefficients of window $v(\cdot)$. Notice that the computation of (18) relies only on real numbers, while in the classic TFT the elements of $\mathcal{M}(\cdot)$ are complex-valued [25], [35]. As a result, in the former case the total number of arithmetic operations is much lower, with a consequent reduction in computation time, as it will be shown in Section V.

As far as the number of model terms is concerned, in the classic TFT, H is assumed to be arbitrarily large and the order of the Taylor's series is the same for all harmonics. In principle, setting H as large as possible is motivated by the fact that numerous harmonics (up to the 50th in the IEEE Standards) may affect power system waveforms. However, in practice their impact on the estimation of the fundamental tone parameters tends to decrease as the harmonic order grows [44]. This behavior is not clearly visible when $v(\cdot)$ is a rectangular window due to its relevant spectral leakage, but it becomes more noticeable when two-term cosine-class windows are used. In general, the actual impact of harmonics on synchrophasor estimation accuracy depends not only on their order and magnitude, but also on observation interval length. This affects the width of the spectral main-lobes and side-lobes associated with the various waveform harmonic components, regardless of the number of terms estimated through (18). When shorter intervals are considered, a larger number of terms has to be included in (14) to ensure that harmonics have a negligible impact on fundamental tone parameters estimation. In particular, it was heuristically verified through simulations that estimation results in the presence of harmonics do not change significantly if

- $H\geq 4$ for $C=2$;
- $H\geq 3$ for $C=\{3,4\}$;
- $H\geq 2$ for $C=\{5,6,7\}$.

Therefore, in the TLTFT H is set as little as possible for a given observation interval duration, as shown in Fig. 1. Moreover, since harmonic distortion is often dominated by steady-state contributions (as it is implicitly supposed in the IEEE Standards as well), tracking harmonics over time is usually unnecessary. Hence, to further limit the computational burden, the Taylor's series of the harmonic terms can be truncated to order 0, i.e. $K_h=0$, for $h>1$. On the contrary, at least the first- and second-order coefficients of the the Taylor's series of $X^{(1)}$ are needed (i.e. $K_1=2$) to estimate not only amplitude and phase, but also frequency and ROCOF of the fundamental tone. In particular, the fundamental synchrophasor magnitude, phase, frequency and ROCOF at time t_r are given respectively by [45]:

$$\begin{aligned}\hat{X}(t_r)&=\sqrt{\hat{X}_{R_0}^{(1)^2}+\hat{X}_{I_0}^{(1)^2}}\\ \hat{\varphi}(t_r)&=\mathrm{atan}\frac{\hat{X}_{I_0}^{(1)}}{\hat{X}_{R_0}^{(1)}}\\ \hat{f}(t_r)&=f_0(1+\hat{\delta})+\frac{f_s}{2\pi}\frac{\hat{X}_{R_0}^{(1)}\hat{X}_{I_1}^{(1)}-\hat{X}_{I_0}^{(1)}\hat{X}_{R_1}^{(1)}}{|\hat{X}(t_r)|^2}\\ \widehat{ROCOF}(t_r)&=\frac{f_s^2}{\pi}\left[\frac{\hat{X}_{R_0}^{(1)}\hat{X}_{I_2}^{(1)}-\hat{X}_{I_0}^{(1)}\hat{X}_{R_2}^{(1)}}{|\hat{X}(t_r)|^2}-\right.\\ &\left.\frac{(\hat{X}_{R_0}^{(1)}\hat{X}_{R_1}^{(1)}+\hat{X}_{I_0}^{(1)}\hat{X}_{I_1}^{(1)})(\hat{X}_{R_0}^{(1)}\hat{X}_{I_1}^{(1)}-\hat{X}_{I_0}^{(1)}\hat{X}_{R_1}^{(1)})}{|\hat{X}(t_r)|^4}\right].\end{aligned} \tag{19}$$

IV. Accuracy Tests and Results

The accuracy of the TLTFT algorithm has been analyzed in different *Class P* and *Class M* testing conditions reported in the IEEE Standards C37.118.1-2011 and C37.118.1a-2014 [21], [24], i.e.

- When the fundamental has either amplitude between 80% and 120% of the nominal value and frequency $f=50\pm 2$ Hz (for *Class P*) or amplitude between 10% and 120% of the nominal value and frequency $f=50\pm 5$ Hz (for *Class M*) (*case a*);
- Under the effect of a chirp waveform with frequency changing linearly from about 48 Hz to 52 Hz (for *Class*

P) or from about 45 Hz to 55 Hz (for *Class M*) and vice versa at a rate of ± 1 Hz/s (*case b*);
- When the waveform is affected by both off-nominal frequency deviations within ± 2 Hz or ± 5 Hz (as specified above) and steady-state harmonics, taken one at a time, of amplitude equal to 1% (*Class P*) or 10% (*Class M*) of the reference value (*cases c*, *d* and *e*, for second, third and fourth harmonic, respectively);
- Under the influence of a sinusoidal amplitude modulation (AM) of magnitude equal to 10% of the fundamental and frequency equal to 2 Hz (for *Class P*) or 5 Hz (for *Class M*) (*case f*);
- Under the influence of a sinusoidal phase modulation (PM) of amplitude equal to 0.1 rad and frequency equal to 2 Hz (for *Class P*) or 5 Hz (for *Class M*) (*case g*);
- Under the influence of a single out-of-band interharmonic of amplitude equal to 10% of the fundamental in the frequency intervals [10, 25] Hz and [75, 100] Hz, assuming that the PMU reporting rate is 50 frame/s (*case h* for *Class M* PMUs only).

This section reports both simulation and experimental results in each one of the testing conditions specified above. The rationale for comparing simulation and experimental results is twofold. On one hand, it provides a confirmation of the correct behavior of the estimation algorithm even in the presence of additional uncertainty contributions (mainly due to transducers as well as signal conditioning, data acquisition and synchronization circuitry), which can be hardly modeled and included in simulations. On the other hand, it helps to evaluate to what extent such contributions, in the best case, can affect the overall measurement accuracy.

In both simulations and experiments, the MIR window has been used not only within the IpDFT, but also in the subsequent real-valued TFT (i.e. $w(\cdot) = v(\cdot)$). This choice is due to the fact, that, after trying different window functions, this solution provides the best trade-off between accuracy and responsiveness.

The Monte Carlo simulations have been performed in Matlab assuming a sampling rate $f_s = 8$ kHz and a Signal-to-noise Ratio (SNR) equal to 80 dB. Multiple values of TVE, FE and RFE at different reference times have been computed by using noisy waveforms of different duration in the *cases a–h* listed above. Every kind of test has been repeated about 200 times changing randomly the initial phases of both the fundamental component and the various disturbances considered (i.e. harmonics, inter-harmonics or modulating tones) in $[0, 2\pi)$. As known, for *Class P* PMUs responsiveness is more important than accuracy. Therefore, shorter observation intervals (i.e. consisting of $C = \{2, 3, 4\}$ nominal waveform cycles) have been chosen for *Class P* testing. On the contrary, intervals including $C = \{5, 6, 7\}$ cycles have been considered for *Class M* testing, since in this case measurement accuracy has a higher relevance.

The experiments in the same testing conditions *a–h* listed at the beginning of this Section, have been performed in the laboratories of the University "L. Vanvitelli" in Aversa, Italy, using

- A calibrator Fluke 6135A/PMUCAL [46];
- A resistive voltage transducer with a rated ratio of 65 V/V;
- A PXI system equipped with a 16-bit multi-functional NI PXIe-6124 data acquisition (DAQ) module and a time synchronization module NI PXI 6683H.

The Fluke 6135A/PMUCAL is able to generate three-phase voltages up to 1000 V and three-phase currents up to 21 A. However, for the purpose of this paper, only a single-phase voltage waveform has been used for testing. The adopted voltage transducer is a resistive divider made up of two precision decade resistors. The total resistance of the divider is 65 kΩ. The voltage transducer has been properly calibrated, as described in [47], [48], to compensate systematic ratio and phase deviations. Moreover, an output parallel capacitor is used to realize a first-order lowpass filter with a cut-off frequency at about 5 kHz to improve the Signal-To-Noise-and-Distortion (SINAD) at the input of the DAQ module. In this way, the SINAD of the collected waveform in nominal conditions (i.e. without including other disturbances) is about 70 dB. The sampling frequency f_s of the DAQ module is set to 8 kHz, like in simulations. The NI PXI 6683H module synchronizes both the clock sampling signal and the data acquisition module. In the case at hand, the UTC time reference is an IRIG-B signal generated by the calibrator. The software for instrument control, data acquisition and data post-processing is written in LabVIEW. In this case, the TLTFT algorithm has been implemented in C++ using the Eigen[1] open source library for optimized linear algebra operations. The TLTFT routines (compiled with Visual Studio 2017 as a dynamic link library – DLL) is called directly in the LabVIEW Virtual Instrument (VI) through code library function nodes.

Tabs. I and II report the maximum values of TVE, FE and RFE computed over hundreds of repeated simulations (a) and experiments (b) in the *Class P* and *Class M* testing conditions labeled as *a–h*. The results with harmonics of order higher than the fourth are generally very close to those of *case e*. Therefore, they are not reported for the sake of brevity. First of all, it is interesting to highlight that simulation and experimental results are generally quite consistent. This is a remarkable result, as it confirms that the uncertainty contributions due to transducers, acquisition and synchronization circuitry can be reasonably kept under control. Therefore, in the best case, the theoretical accuracy of the TLTFT algorithm is within reach. Despite this, the impact of measurement transducers on experimental results could be critical. Indeed, it has been observed that the nuisances caused by transducers made by different manufacturers may drastically affect measurement results even if the systematic deviations are estimated and compensated, thus blurring the accuracy analysis.

The results in Tab. I(a)-(b) show that the maximum values of TVE, FE and RFE are usually well below the *Class P* standard limits. In Tab. I(b), apparently just in *cases a–e* the experimental RFE values obtained with $C = 2$ exceed the limits. However, this is probably due to the residual uncertainty contributions introduced by the testbed and not to the estimation algorithm per se.

[1] https://www.openhub.net/p/eigen

TABLE I. MAXIMUM TVE, FE AND RFE VALUES OBTAINED THROUGH SIMULATIONS (A) AND EXPERIMENTS (B) IN VARIOUS CLASS P TESTING CONDITIONS REPORTED IN THE IEEE STANDARDS FOR OBSERVATION INTERVALS OF $C = \{2, 3, 4\}$ CYCLES AND $f_s = 8$ KHZ. THE LIMITS OF THE IEEE STANDARD C37.118.1A-2014 FOR A REPORTING RATE OF 50 FPS ARE ALSO SHOWN FOR COMPARISON.

Case	Test type	TVE [%]				FE [mHz]				RFE [Hz/s]			
		Limit	C=2	C=3	C=4	Limit	C=2	C=3	C=4	Limit	C=2	C=3	C=4
a	Freq. offset (± 2 Hz) and amplitude within $[0.8, 1.2]$ p.u.	1	0.00	0.00	0.00	5	0.3	0.3	0.2	0.4	0.10	0.04	0.02
b	Freq. ramp (± 2 Hz at 1 Hz/s)	1	0.00	0.00	0.00	10	0.4	0.3	0.2	0.4	0.11	0.03	0.02
c	Freq. offset (± 2 Hz) + 1% 2nd harmonic	1	0.00	0.00	0.00	5	0.9	0.2	0.1	0.4	0.18	0.04	0.02
d	Freq. offset (± 2 Hz) + 1% 3rd harmonic	1	0.00	0.00	0.00	5	0.6	0.3	0.1	0.4	0.19	0.04	0.02
e	Freq. offset (± 2 Hz) + 1% 4th harmonic	1	0.00	0.00	0.00	5	0.5	0.3	0.1	0.4	0.12	0.04	0.02
f	AM (10% at 2 Hz)	3	0.00	0.00	0.00	60	0.3	0.2	0.2	2.3	0.15	0.03	0.01
g	PM (0.1 rad. at 2 Hz)	3	0.00	0.00	0.00	60	0.8	1.3	1.9	2.3	0.13	0.04	0.03

(a)

Case	Test type	TVE [%]				FE [mHz]				RFE [Hz/s]			
		Limit	C=2	C=3	C=4	Limit	C=2	C=3	C=4	Limit	C=2	C=3	C=4
a	Freq. offset (± 2 Hz) and amplitude within $[0.8, 1.2]$ p.u.	1	0.02	0.02	0.02	5	1.8	0.7	0.4	0.4	0.78	0.13	0.05
b	Freq. ramp (± 2 Hz at 1 Hz/s)	1	0.02	0.02	0.02	10	1.8	0.6	0.4	0.4	0.55	0.14	0.04
c	Freq. offset (± 2 Hz) + 1% 2nd harmonic	1	0.02	0.02	0.02	5	2.2	0.6	0.4	0.4	0.88	0.15	0.04
d	Freq. offset (± 2 Hz) + 1% 3rd harmonic	1	0.02	0.02	0.02	5	2.1	0.6	0.4	0.4	0.72	0.13	0.04
e	Freq. offset (± 2 Hz) + 1% 4th harmonic	1	0.02	0.02	0.01	5	1.8	0.6	0.5	0.4	0.68	0.17	0.05
f	AM (10% at 2 Hz)	3	0.02	0.02	0.02	60	0.8	0.6	0.4	2.3	0.70	0.16	0.04
g	PM (0.1 rad. at 2 Hz)	3	0.02	0.02	0.02	60	1.9	1.5	2.0	2.3	0.20	0.08	0.06

(b)

TABLE II. MAXIMUM TVE, FE AND RFE VALUES OBTAINED THROUGH SIMULATIONS (A) AND EXPERIMENTS (B) IN VARIOUS CLASS M TESTING CONDITIONS REPORTED IN THE IEEE STANDARDS FOR OBSERVATION INTERVALS OF $C = \{5, 6, 7\}$ CYCLES AND $f_s = 8$ KHZ. THE LIMITS OF THE IEEE STANDARD C37.118.1A-2014 FOR A REPORTING RATE OF 50 FPS ARE ALSO SHOWN FOR COMPARISON.

Case	Test type	TVE [%]				FE [mHz]				RFE [Hz/s]			
		Limit	C=5	C=6	C=7	Limit	C=5	C=6	C=7	Limit	C=5	C=6	C=7
a	Freq. offset (± 5 Hz) and amplitude within $[0.8, 1.2]$ p.u.	1	0.00	0.00	0.00	5	0.1	0.1	0.1	0.1	0.01	0.01	0.01
b	Freq. ramp (± 5 Hz at 1 Hz/s)	1	0.00	0.00	0.00	10	0.3	0.4	0.3	0.2	0.02	0.01	0.01
c	Freq. offset (± 5 Hz) + 10% 2nd harmonic	1	0.00	0.00	0.00	25	0.1	0.1	0.1	–	0.01	0.01	0.00
d	Freq. offset (± 5 Hz) + 10% 3rd harmonic	1	0.00	0.00	0.00	25	0.1	0.1	0.1	–	0.01	0.01	0.01
e	Freq. offset (± 5 Hz) + 10% 4th harmonic	1	0.00	0.00	0.00	25	0.1	0.1	0.1	–	0.01	0.01	0.00
f	AM (10% at 5 Hz)	3	0.04	0.07	0.13	300	3.1	4.6	7.4	14	0.04	0.03	0.06
g	PM (0.1 rad at 5 Hz)	3	0.03	0.07	0.12	300	42	62	79	14	1.2	1.6	2.2
h	10% inter-harmonic within [10,25] Hz and [75,100] Hz	1.3	3.2	1.2	0.19	10	196	34	6.1	–	44	13	1.2

(a)

Case	Test type	TVE [%]				FE [mHz]				RFE [Hz/s]			
		Limit	C=5	C=6	C=7	Limit	C=5	C=6	C=7	Limit	C=5	C=6	C=7
a	Freq. offset (± 5 Hz) and amplitude within $[0.8, 1.2]$ p.u.	1	0.01	0.01	0.01	5	0.2	0.2	0.2	0.1	0.03	0.02	0.01
b	Freq. ramp (± 5 Hz at 1 Hz/s)	1	0.02	0.02	0.02	10	0.3	0.2	0.2	0.2	0.03	0.02	0.01
c	Freq. offset (± 5 Hz) + 10% 2nd harmonic	1	0.01	0.01	0.01	25	0.3	0.2	0.2	–	0.03	0.02	0.01
d	Freq. offset (± 5 Hz) + 10% 3rd harmonic	1	0.01	0.01	0.01	25	0.3	0.2	0.2	–	0.03	0.02	0.01
e	Freq. offset (± 5 Hz) + 10% 4th harmonic	1	0.01	0.01	0.01	25	0.3	0.2	0.2	–	0.03	0.02	0.01
f	AM (10% at 5 Hz)	3	0.06	0.09	0.14	300	3.2	4.9	7.2	14	0.04	0.05	0.07
g	PM (0.1 rad at 5 Hz)	3	0.03	0.07	0.12	300	40	56	75	14	1.2	1.6	2.2
h	10% inter-harmonic within [10,25] Hz and [75,100] Hz	1.3	3.2	1.2	0.12	10	196	33	6.5	–	44	13	1.2

(b)

The results in Tab. II(a)-(b) for *Class M* testing generally confirm those in Tab. I(a)-(b). Observe that the *Class M* ROCOF accuracy requirements are partially undefined, since some RFE limits have been suspended in [24]. As a general rule, using longer observation intervals reduces the impact of steady-state disturbances (particularly harmonics and inter-harmonics). Moreover, the maximum TVE, FE and RFE values are smaller than or at most comparable with those shown in Tab. I(a)-(b), even if the harmonics magnitude is 10 times larger than in *Class P* testing and the number of harmonics modeled in the algorithm is lower ($H = 2$). These results suggest that for $C > 4$ it is pointless to include harmonics higher than the second in (14). However, as C increases the sensitivity to AM, and particularly, to PM grows. This is a known issue due to the fact that the approximation errors of the synchrophasor Taylor's series increases with the distance from the central reference time. Nevertheless, the IEEE Standard limits (which are less strict in *cases f* and g than in steady-state conditions) are safely met. As, expected, the most critical results are obtained under the effect of out-of-band inter-harmonics particularly when they are closer to the passband (i.e. at about 25 Hz and 75 Hz if the reporting rate is set to 50 frame/s). Under this testing condition, the maximum TVE, FE and RFE values are below the limits of the IEEE Standard C37.118.1a-2014 only for $C = 7$. Quite interestingly, in this case experimental and simulation-based results are perfectly consistent.

To complete the analysis, further experiments have been

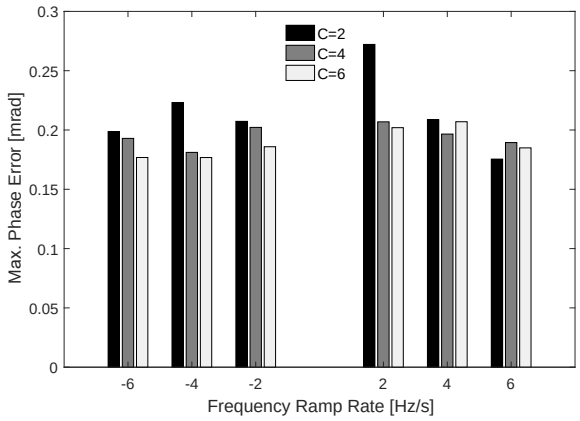

Fig. 2. Experimental maximum phase estimation errors when the test waveform frequency changes linearly between about 45 Hz and 55 Hz and vice versa at different rates.

conducted to evaluate just the phase estimation accuracy. As explained in Section I, the angle differences between voltage bus and current branch phasors at the distribution level are expected to be extremely small, i.e. in the order of a few mrad or less. The results of most of the testing conditions specified in the IEEE Standards have shown that the TLTFT algorithm is generally able to meet this requirement, as confirmed by the small TVE values shown in Tabs. I and II. Since the case of dynamic disturbances is probably more interesting for active distribution networks, Fig. 2 explicitly shows the experimental maximum phase estimation errors for $C = 2$, $C = 4$ and $C = 6$ (i.e. using $H = 4$, $H = 3$ and $H = 2$ harmonics, respectively, in the system model) when the waveform frequency changes linearly from about 45 Hz to 55 Hz and vice versa at different rates (e.g. ± 2, ± 4 and ± 6 Hz/s). In all cases, the maximum phase estimation errors range between 0.2 and 0.3 mrad, with minor fluctuations that are quite independent of the frequency ramp rate and are probably due to the uncertainty contributions introduced by the measurement testbed.

V. Embedded Implementation and Processing Time Analysis

The C++ implementation of the TLTFT algorithm has been compiled with GCC v4.6.3 in release mode (i.e. without the debug data that tend to slow down software execution) to be ported on a Beagle-Bone Black board (BBB). This is a low-cost embedded development platform, which has been recently used to develop the acquisition and synchronization stages of a prototype PMU within the OpenPMU project [49]. The goal of the research reported in this paper is complementary to [49], as it shows that not only acquisition and synchronization functions, but also waveform parameters estimation can be successfully and effectively implemented using low-cost embedded systems. The BBB platform is equipped with an Angstrom Linux distribution with kernel v4.4 patched for real-time operation. The board consists of a 32-bit 1-GHz Sitara ARM Cortex-A8 Central Processing Unit (CPU) with 512 MB DDR3 SDRAM memory, and up to 4 GB on-board flash memory. One key advantage of the BBB over other embedded platforms is the presence of two additional 32-bit 200-MHz Programmable Real-time Units (PRUs). The PRUs can be configured as co-processors to run time-critical portions of a given software application (e.g. for data streaming). Each PRU is equipped with 8 kB of RAM data memory and has a direct access to peripherals. PRUs and the main processor share 12 kB of RAM memory for data communication. The BBB platform includes two 46-pin headers for General Purpose Input-Output (GPIO) connections, USB ports, a micro HDMI connector for audio/video output, and a 10/100 Ethernet port.

The processing time of the TLTFT estimator has been measured with low-level software timers (i.e. through the *clock* function of the standard C library) for different possible sampling rates between 2 kHz and 12 kHz, with observation intervals ranging from 2 to 7 nominal waveform cycles, in line with the experiments described in Section IV. The maximum processing times computed over 100 iterations of the TLTFT algorithm are shown in Fig. 3 as a function of the sampling frequency. In general, they are quite deterministic, i.e. they exhibit minor fluctuations over multiple iterations. In all cases the curves exhibits approximately a linear trend. This result is consistent with the order of complexity of both the IpDFT and the TFT, which grows linearly with the total number of samples N. Observe that the processing time values obtained with $C = 4$ and $C = 5$ are very close. This apparently weird result is due to the fact that in the former case $H = 3$, whereas in the latter $H = 2$. As a result, the size of matrix (15) changes as well. Since the order of complexity of (18) depends cubically on the number of columns of (15), the higher computational burden due to a larger data record when $C = 5$ is almost perfectly compensated by model complexity reduction. A similar situation occurs between $C = 2$ and $C = 3$, namely when the number of estimated harmonics H switches from 4 to 3. However, in this case the reduction in model complexity just partially counterbalances the processing burden increment caused by the larger record size. Therefore, the lines associated with the maximum processing times in Fig. 3 are farther apart. The dashed horizontal lines at 20 ms and 16.7 ms represent the upper bounds to processing time needed to ensure that the PMU reporting rates reach the maximum mandatory values specified in the IEEE Standards, i.e. 50 frame/s when $f_0 = 50$ Hz and 60 frame/s when $f_0 = 60$ Hz, respectively. Observe that with $f_s = 8$ kHz (as it was assumed in Section IV) a reporting rate of 50 frame/s can be safely achieved even with $C = 7$. To assure a reporting rate of 60 frame/s over 7 cycles, the sampling frequency should be slightly reduced (e.g. $f_s = 7$ kHz). However, this change does not affect accuracy significantly. It is interesting to highlight that in the C++ implementation of the TLTFT algorithm for the BBB platform, all floating point variables are defined as *float* (i.e. single precision) to fully exploit the 32-bit data path of the available floating point units. This choice slightly degrades accuracy with respect to the results shown in Section IV. However, processing times are about 35% shorter on average than using double-precision variables.

Finally, the bar diagram in Fig. 4 shows a comparison

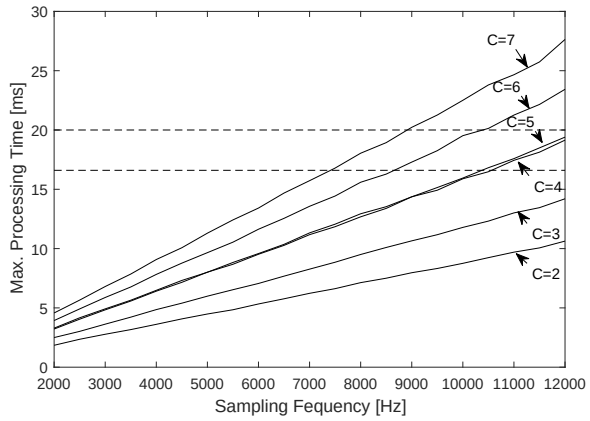

Fig. 3. Maximum processing times of the TLTFT algorithm as a function of the sampling frequency f_s and for different values of C. The dashed horizontal lines represent the time limits that should be met to achieve the highest mandatory reporting rates reported in the IEEE Standards, i.e. 50 frame/s when $f_0 = 50$ Hz and 60 frame/s when $f_0 = 60$ Hz.

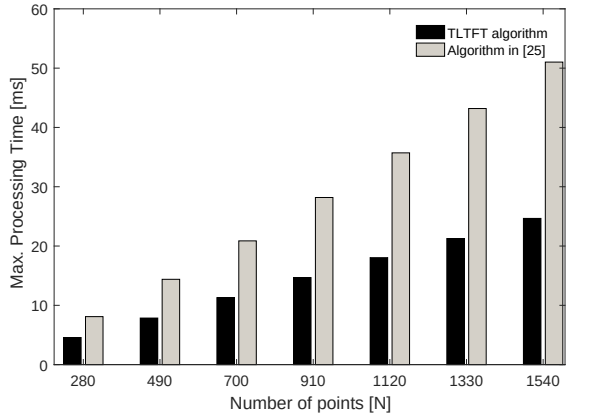

Fig. 4. Maximum processing times of the TLTFT versus the algorithm in [25] for different number of samples N and $C = 7$.

between the maximum processing times of the TLTFT and those obtained with the algorithm described in [25], as a function of the number of samples N in the worst case, namely when $C = 7$. Clearly, the TLTFT is much faster than the algorithm in [25], as the processing time is reduced by $50\% \pm 2\%$. This is due to the fact that the estimator in [25] relies on a classic, complex-valued TFT, with both real and imaginary parts represented as float variables and with $H = 3$ in all cases. Over shorter observation intervals, the relative speed improvement is a bit lower. However, it is still about 40% on average and never smaller than about 25%.

VI. Conclusions

This paper presents an estimation algorithm for Phasor Measurement Units (PMUs) suitable to be implemented on low-cost processing platforms. The adopted technique results from the tailored combination and optimization of two state-of-the-art algorithms, i.e. an Interpolated DFT (IpDFT) along with a preliminary bandpass filter and a real-valued Taylor-Fourier Transform (TFT). The IpDFT is applied to the filtered waveform to estimate the fundamental static off-nominal frequency deviation, which in turn is used to tune the coefficients of the TFT matrix. The TFT consists of a flexible number of harmonic terms which decreases with the observation interval length, and it is applied to the unfiltered waveform in order to track synchrophasor, fundamental frequency and ROCOF changes over time.

The algorithm, implemented on a BeagleBone Black board, is potentially able to return estimates at reporting rates compliant with the mandatory requirements of the IEEE Standards C37.118.1-2011 when the sampling range is up to 8 kHz.

The experimental data obtained using a PMU calibrator are generally consistent with the respective simulation results and show a good compliance with most of the *Class P* and *Class M* accuracy requirements specified in the IEEE Standard C37.118.1-2011 and the Amendment C37.118.1a-2014, although different transducers can strongly and unpredictably affect measurement results. Phase estimation accuracy is smaller than 1 mrad in most testing conditions, which is very important for distribution system monitoring.

References

[1] A. G. Phadke, J. S. Thorp, and M. G. Adamiak, "A new measurement technique for tracking voltage phasors, local system frequency, and rate of change of frequency," *IEEE Transactions on Power Apparatus and Systems*, vol. PAS-102, no. 5, pp. 1025–1038, May 1983.

[2] A. G. Phadke, J. S. Thorp, and K. J. Karimi, "State estimation with phasor measurements," *IEEE Transactions on Power Systems*, vol. 1, no. 1, pp. 233–238, Feb. 1986.

[3] W. Sattinger and G. Giannuzzi, "Monitoring continental europe: An overview of WAM systems used in italy and switzerland," *IEEE Power and Energy Magazine*, vol. 13, no. 5, pp. 41–48, Sep. 2015.

[4] P. Castello, P. Ferrari, A. Flammini, C. Muscas, P. A. Pegoraro, and S. Rinaldi, "A distributed PMU for electrical substations with wireless redundant process bus," *IEEE Transactions on Instrumentation and Measurement*, vol. 64, no. 5, pp. 1149–1157, May 2015.

[5] M. Pignati, L. Zanni, P. Romano, R. Cherkaoui, and M. Paolone, "Fault detection and faulted line identification in active distribution networks using synchrophasors-based real-time state estimation," *IEEE Transactions on Power Delivery*, vol. 32, no. 1, pp. 381–392, Feb. 2017.

[6] A. Moschitta, P. Carbone, and C. Muscas, "Performance comparison of advanced techniques for voltage dip detection," *IEEE Transactions on Instrumentation and Measurement*, vol. 61, no. 5, pp. 1494–1502, May 2012.

[7] A. M. Dumitrescu, R. Roman, and M. Albu, "Synchronized measurements and power quality assesment," in *2015 IEEE Eindhoven PowerTech*, Eindhoven, Netherlands, Jun. 2015, pp. 1–6.

[8] D. Macii, D. Fontanelli, and D. Petri, "Performance of phasor measurement units for power quality event detection in urban distribution grids," in *Proc. IEEE International Smart Cities Conference (ISC2)*, Trento, Italy, Sep. 2016, pp. 1–7.

[9] J. Liu, J. Tang, F. Ponci, A. Monti, C. Muscas, and P. A. Pegoraro, "Trade-offs in PMU deployment for state estimation in active distribution grids," *IEEE Transactions on Smart Grid*, vol. 3, no. 2, pp. 915–924, Jun. 2012.

[10] M. H. F. Wen, J. Xu, and V. O. K. Li, "Optimal multistage PMU placement for wide-area monitoring," *IEEE Transactions on Power Systems*, vol. 28, no. 4, pp. 4134–4143, Nov. 2013.

[11] K. G. Khajeh, E. Bashar, A. M. Rad, and G. B. Gharehpetian, "Integrated model considering effects of zero injection buses and conventional measurements on optimal PMU placement," *IEEE Transactions on Smart Grid*, vol. 8, no. 2, pp. 1006–1013, Mar. 2017.

[12] R. Brown, "Impact of smart grid on distribution system design," in *Proc. IEEE Power and Energy Society General Meeting*, Pittsburgh, PA, USA, Jul. 2008, pp. 1–4.

[13] A. Borghetti, C. Nucci, M. Paolone, G. Ciappi, and A. Solari, "Synchronized phasors monitoring during the islanding maneuver of an active distribution network," *IEEE Transactions on Smart Grid*, vol. 2, no. 1, pp. 82–91, Mar. 2011.

[14] L. Peretto, "The role of measurements in the smart grid era," *IEEE Instrumentation Measurement Magazine*, vol. 13, no. 3, pp. 22–25, Jun. 2010.

[15] P. Romano and M. Paolone, "Enhanced Interpolated-DFT for synchrophasor estimation in FPGAs: Theory, implementation, and validation of a PMU prototype," *IEEE Transactions on Instrumentation and Measurement*, vol. 63, no. 12, pp. 2824–2836, Dec. 2014.

[16] G. Barchi, D. Fontanelli, D. Macii, and D. Petri, "On the accuracy of phasor angle measurements in power networks," *IEEE Transactions on Instrumentation and Measurement*, vol. 64, no. 5, pp. 1129–1139, May 2015.

[17] A. von Meier, D. Culler, A. McEachern, and R. Arghandeh, "Micro-synchrophasors for distribution systems," in *IEEE PES Innovative Smart Grid Technologies Conference (ISGT)*, Washington, DC, USA, Feb. 2014, pp. 1–5.

[18] S. Kon and T. Yamada, "Frequency characterizations of voltage and current transducers for evaluation of phasor measurement units," in *Proc. IEEE 10th International Conference on Power Electronics and Drive Systems (PEDS)*, Kitakyushu, Japan, Apr. 2013, pp. 989–991.

[19] G. Crotti, D. Gallo, D. Giordano, C. Landi, and M. Luiso, "A characterized method for the real-time compensation of power system measurement transducers," *IEEE Transactions on Instrumentation and Measurement*, vol. 64, no. 6, pp. 1398–1404, Jun. 2015.

[20] L. Peretto, R. Tinarelli, and K. Yiit, "Uncertainty evaluation in measurement equipments for power systems," in *Proc. IEEE International Workshop on Applied Measurements for Power Systems (AMPS)*, Aachen, Germany, Sep. 2016, pp. 1–5.

[21] "IEEE standard for synchrophasor measurements for power systems," *IEEE Std. C37.118.1-2011*, pp. 1–61, Dec. 2011.

[22] "IEEE standard for synchrophasor data transfer for power systems," *IEEE Std. C37.118.2-2011*, pp. 1–53, Dec. 2011.

[23] B. Ristic and B. Boashash, "Comments on "the Cramer-Rao lower bounds for signals with constant amplitude and polynomial phase"," *IEEE Transactions on Signal Processing*, vol. 46, no. 6, pp. 1708–1709, Jun. 1998.

[24] "IEEE standard for synchrophasor measurements for power systems – amendment 1: Modification of selected performance requirements," *IEEE Std C37.118.1a-2014 (Amendment to IEEE Std C37.118.1-2011)*, pp. 1–25, Apr. 2014.

[25] P. Tosato, D. Macii, and D. Brunelli, "Implementation of phasor measurement units on low-cost embedded platforms: a feasibility study," in *Proc. IEEE International Instrumentation and Measurement Technology Conference (I2MTC)*, Turin, Italy, May 2017, pp. 1–6.

[26] D. Macii, D. Petri, and A. Zorat, "Accuracy analysis and enhancement of DFT-based synchrophasor estimators in off-nominal conditions," *IEEE Transactions on Instrumentation and Measurement*, vol. 61, no. 10, pp. 2653–2664, Oct. 2012.

[27] D. Belega and D. Petri, "Accuracy analysis of the multicycle synchrophasor estimator provided by the interpolated DFT algorithm," *IEEE Transactions on Instrumentation and Measurement*, vol. 62, no. 5, pp. 942–953, May 2013.

[28] D. Macii, G. Barchi, and D. Petri, "Design criteria of digital filters for synchrophasor estimation," in *Proc. IEEE International Instrumentation and Measurement Technology Conference (I2MTC)*, Minneapolis, MN, USA, May 2013, pp. 1579–1584.

[29] A. Roscoe, I. Abdulhadi, and G. Burt, "P and M class phasor measurement unit algorithms using adaptive cascaded filters," *IEEE Transactions on Power Delivery*, vol. 28, no. 3, pp. 1447–1459, Jul. 2013.

[30] A. J. Roscoe, B. Dickerson, and K. E. Martin, "Filter design masks for C37.118.1a-compliant frequency-tracking and fixed-filter M-Class phasor measurement units," *IEEE Transactions on Instrumentation and Measurement*, vol. 64, no. 8, pp. 2096–2107, Aug. 2015.

[31] M. Platas-Garza and J. de la O Serna, "Dynamic phasor and frequency estimates through maximally flat differentiators," *IEEE Transactions on Instrumentation and Measurement*, vol. 59, no. 7, pp. 1803–1811, Jul. 2010.

[32] P. Castello, J. Liu, C. Muscas, P. A. Pegoraro, F. Ponci, and A. Monti, "A fast and accurate PMU algorithm for P+M class measurement of synchrophasor and frequency," *IEEE Transactions on Instrumentation and Measurement*, vol. 63, no. 12, pp. 2837–2845, Dec. 2014.

[33] W. Premerlani, B. Kasztenny, and M. Adamiak, "Development and implementation of a synchrophasor estimator capable of measurements under dynamic conditions," *IEEE Transactions on Power Delivery*, vol. 23, no. 1, pp. 109–123, Jan. 2008.

[34] D. Petri, D. Fontanelli, and D. Macii, "A frequency-domain algorithm for dynamic synchrophasor and frequency estimation," *IEEE Transactions on Instrumentation and Measurement*, vol. 63, no. 10, pp. 2330–2340, Oct. 2014.

[35] M. A. Platas-Garza and J. A. de la O Serna, "Dynamic harmonic analysis through Taylor-Fourier transform," *IEEE Transactions on Instrumentation and Measurement*, vol. 60, no. 3, pp. 804–813, Mar. 2011.

[36] M. D. Kušljevìc and J. J. Tomìc, "Multiple-resonator-based power system Taylor-Fourier harmonic analysis," *IEEE Transactions on Instrumentation and Measurement*, vol. 64, no. 2, pp. 554–563, Feb. 2015.

[37] J. A. de la O Serna and J. Rodriguez-Maldonado, "Instantaneous oscillating phasor estimates with Taylor^K-Kalman filters," *IEEE Transactions on Power Systems*, vol. 26, no. 4, pp. 2336–2344, Nov 2011.

[38] J. Liu, F. Ni, J. Tang, F. Ponci, and A. Monti, "A Modified Taylor-Kalman Filter for Instantaneous Dynamic Phasor Estimation," in *2012 3rd IEEE PES Innovative Smart Grid Technologies Europe (ISGT Europe)*, Berlin, Germany, Oct. 2012, pp. 1–7.

[39] R. Ferrero, P. A. Pegoraro, and S. Toscani, "Dynamic Fundamental and Harmonic Synchrophasor Estimation by Extended Kalman Filter," in *Proc. IEEE International Workshop on Applied Measurements for Power Systems (AMPS)*, Aachen, Germany, Sep. 2016, pp. 1–6.

[40] D. Fontanelli, D. Macii, and D. Petri, "Dynamic synchrophasor estimation using smoothed Kalman filtering," in *2016 IEEE International Instrumentation and Measurement Technology Conference Proceedings*, Taipei, Taiwan, May 2016, pp. 1–6.

[41] M. Bertocco, G. Frigo, G. Giorgi, and C. Narduzzi, "Frequency tracking for efficient phasor measurement based on a CSTFM model," in *Proc. IEEE International Workshop on Applied Measurements for Power Systems (AMPS)*, Aachen, Germany, Sep. 2015, pp. 84–89.

[42] D. Macii, D. Fontanelli, G. Barchi, and D. Petri, "Impact of acquisition wideband noise on synchrophasor measurements: A design perspective," *IEEE Transactions on Instrumentation and Measurement*, vol. 65, no. 10, pp. 2244–2253, Oct. 2016.

[43] D. Belega, D. Macii, and D. Petri, "Fast synchrophasor estimation by means of frequency-domain and time-domain algorithms," *IEEE Transactions on Instrumentation and Measurement*, vol. 63, no. 2, pp. 388–401, Feb. 2014.

[44] G. Barchi, D. Macii, and D. Petri, "Synchrophasor estimators accuracy: a comparative analysis," *IEEE Transactions on Instrumentation and Measurement*, vol. 62, no. 5, pp. 963–973, May 2013.

[45] D. Belega and D. Petri, "A real-valued taylor weighted least squares synchrophasor estimator," in *2014 IEEE International Workshop on Ap-*

plied Measurements for Power Systems Proceedings (AMPS), Aachen, Germany, Sep. 2014, pp. 1–6.

[46] "Fluke 6135a/pmucal." [Online]. Available: http://us.flukecal.com/products/electrical-calibration/electrical-calibrators/6135apmucal-phasor-measurement-unit-calibrati

[47] G. Crotti, D. Gallo, D. Giordano, C. Landi, M. Luiso, C. Cherbaucich, and P. Mazza, "Low cost measurement equipment for the accurate calibration of voltage and current transducers," in *Proc. IEEE International Instrumentation and Measurement Technology Conference (I2MTC)*, Montevideo, Uruguay, May 2014, pp. 202–206.

[48] G. Crotti, D. Gallo, D. Giordano, C. Landi, and M. Luiso, "Industrial comparator for smart grid sensor calibration," *IEEE Sensors Journal*, vol. PP, no. 99, pp. 1–1, 2017.

[49] X. Zhao, D. M. Laverty, A. McKernan, D. J. Morrow, K. McLaughlin, and S. Sezer, "GPS-disciplined analog-to-digital converter for phasor measurement applications," *IEEE Transactions on Instrumentation and Measurement*, vol. 66, pp. 1–9, 2017.